processes

MDPI

Article

Adaptive Coordinated Optimization and Dispatch of a PV–BESS Under Highly Variable Weather Conditions

Binkai Zhang [1], Wei Li [2,*], Yifan Bian [3], Lirong Xie [3,*], Jiao Ji [1], Jie Hou [4] and Mamadsho Ilolov [5]

[1] College of Intelligent Science and Technology, Xinjiang University, Urumqi 830017, China
[2] Economic and Technological Research Institute, State Grid Xinjiang Electric Power Co., Ltd., Urumqi 830002, China
[3] College of Electrical Engineering, Xinjiang University, Urumqi 830017, China
[4] College of Automation, Chongqing University of Posts and Telecommunications, Chongqing 400065, China
[5] Center of Innovative Development of Science and New Technologies, National Academy of Sciences of Tajikistan, Dushanbe 734025, Tajikistan
* Correspondence: liwei_xjjyy@163.com (W.L.); xielirong@xju.edu.cn (L.X.)

Abstract

To address significant photovoltaic (PV) power fluctuations, large forecast errors, and differences in the operating states of battery energy storage system (BESS) units under highly variable weather conditions, this study proposes an adaptive coordinated optimization and dispatch method for a PV–BESS. Rolling-horizon optimization is first used to generate the total BESS control command. Elastic-net regularization and an abrupt-change protection mechanism are then introduced to decompose the command into a low-frequency smooth component, a high-frequency dynamic component, and a sparse anomaly component. Based on the decomposition results, state-aware power allocation is performed considering the state of charge, state of health, warning state, and fault status of each BESS unit. The updated available power and energy limits are fed back to the rolling optimization model to form a closed-loop coordinated dispatch process. The case study results show that the correlation coefficient between the extracted high-frequency component and the reference dynamic component reaches 0.983. Under the adopted battery degradation model and equivalent operating conditions, the time until the first BESS unit reaches the end-of-life threshold is extended by 13.20% relative to proportional allocation. Under abnormal operating conditions, the proposed method enables warning-state derating, fault isolation, and regulation-task transfer, while dynamic operating-limit feedback reduces unserved command energy by 94.8%. The proposed method improves tracking of the grid power schedule while coordinating the requirements for preserving rapid power variations, protecting BESS-unit lifetime, ensuring command executability, and maintaining safe operation under abnormal conditions.

Keywords: photovoltaic–storage system; rolling optimization; robust decomposition; state-aware allocation; dynamic operating-limit feedback

Check for updates

Academic Editor: Osvaldo José Venturini

Received: 3 September 2026
Revised: 26 September 2026
Accepted: 30 September 2026
Published: 1 October 2026

Copyright: © 2026 by the authors. Licensee MDPI, Basel, Switzerland. This article is an open access article distributed under the terms and conditions of the Creative Commons Attribution (CC BY) license.

1. Introduction

Against the backdrop of China's carbon peaking and carbon neutrality goals and the development of new power systems, the installed capacity of photovoltaic (PV) power generation has continued to increase. However, PV power is inherently intermittent and stochastic. Under highly variable weather conditions, rapidly moving clouds may cause abrupt changes in solar irradiance, thereby increasing PV power forecasting errors

and short-term fluctuations [1,2]. Meanwhile, low ambient temperatures and long-term cycling can reduce the available capacity and operational reliability of battery energy storage systems (BESSs). Consequently, PV–BESS systems must simultaneously meet multiple operational requirements, including tracking of the grid power schedule, PV energy utilization, and safe BESS operation [3–5]. Coordinating these requirements is therefore essential for improving the operational performance of PV power plants equipped with BESSs.

BESSs can compensate for PV power forecasting errors and mitigate output fluctuations through coordinated charging and discharging. Elkazaz et al. [6] proposed a model-predictive-control-based energy management strategy for a PV–wind–battery microgrid, in which operational decisions are continuously optimized by updating forecast information over a rolling horizon. Syed et al. [7] employed a neural-network-based predictive control model to smooth PV power under state-of-charge (SOC) constraints. Yang et al. [8] combined model predictive control with a two-layer fuzzy controller to coordinate tracking of the grid power schedule with BESS state regulation. Lin et al. [9] developed a predictive control model that simultaneously considers grid-connected power smoothing and SOC self-recovery, while accounting for the effects of battery capacity degradation on the long-term performance of hybrid energy storage systems. Bahloul et al. [10] incorporated battery aging costs into PV–BESS scheduling and demonstrated that battery degradation and dispatch performance should be considered jointly. These studies provide a basis for the optimized operation of PV–BESS systems. However, most existing methods focus on generating plant-level power commands, with insufficient consideration of state differences among individual energy storage units and the temporal characteristics of the commands.

The total control command of a BESS generally contains both slowly varying trends and rapidly changing components and may also be corrupted by data-acquisition noise or communication anomalies. In recent years, signal decomposition methods have increasingly been applied to renewable power smoothing and power allocation in hybrid energy storage systems. Huynh et al. [11] employed robust local mean decomposition to extract product functions from solar irradiance time series and characterize their nonlinear and nonstationary variations. Xiao et al. [12] used adaptive variational mode decomposition to separate PV power into different frequency components. Zhang et al. [13] applied an improved variational mode decomposition method to power allocation in hybrid energy storage systems. Wu et al. [14] further indicated that excessive smoothing of genuine power fluctuations should be avoided because it may cause unnecessary battery charging and discharging. Nevertheless, conventional decomposition methods are sensitive to noise, outliers, and parameter settings and may incorrectly identify genuine power variations as anomalous disturbances.

In a multi-unit BESS, individual energy storage units generally differ in SOC, state of health (SOH), and fault status, resulting in different regulation capabilities. The total control command should therefore be allocated according to the actual operating state of each unit. To account for these state differences, Zhang et al. [15] adjusted the power assigned to each unit according to battery state-balancing requirements. Fan et al. [16] developed a rule-based power allocation strategy incorporating battery aging characteristics and initial SOC to reduce the overall aging rate of a multi-unit BESS. Gao et al. [17] optimized power allocation paths according to the degradation ratios of individual units to improve degradation consistency over the full life cycle. References [18,19] employed consensus control and dynamic feedback methods, respectively, to balance SOC while satisfying the total power demand. Chen et al. [20] further incorporated SOC, SOH, temperature, and internal resistance into a coordinated balancing strategy for multiple energy storage units.

Existing power allocation methods mainly determine allocation ratios according to SOC or SOH, while rarely distinguishing between the different effects of low-frequency smooth commands and high-frequency dynamic commands on battery degradation. Moreover, warning and fault conditions are generally handled independently at the execution layer and are not fully fed back to the upper-level rolling optimization process.

To further clarify the differences between the proposed method and existing studies, Table 1 compares representative PV–BESS dispatch and BESS power allocation methods in terms of their main inputs, control strategy and power allocation, degradation consideration, and feedback mechanism.

Table 1. Comparison of representative PV–BESS dispatch and BESS power allocation methods.

Reference	Main Inputs	Control Strategy and Power Allocation	Degradation Consideration	Feedback Mechanism
Elkazaz et al. [6]	Renewable generation, load, and BESS states	Two-stage optimization and predictive control of a centralized BESS	Simplified degradation cost	State feedback to the lower-level controller
Bahloul et al. [10]	PV, BESS, and ancillary-service requirements	Day-ahead linear optimization and plant-level power dispatch	Calendar and cycling aging	Plant-level closed-loop dispatch
Fan et al. [16]	Total power command and unit SOC	Health-aware rule-based power allocation among BESS units	Battery aging function	Unit states used for power allocation
Li et al. [19]	Total power command and unit SOC	Unit power allocation based on dynamic SOC balancing	Indirectly considered through SOC balancing	Dynamic feedback of unit SOC
Proposed method	PV forecast, grid power schedule, and unit states	Rolling-horizon optimization, command decomposition, and state-aware unit allocation	Degradation cost and SOH differences	Operating limits fed back to the upper-level optimization

As shown in Table 1, previous studies have addressed predictive dispatch, degradation-aware optimization, and power allocation among BESS units. However, in the methods compared, plant-level dispatch and unit-level state management are generally handled separately. Few methods jointly consider the decomposition of the total BESS control command and the feedback of updated unit-level operating limits to the upper-level optimization. As a result, plant-level dispatch commands may not fully reflect the actual regulation capability of individual BESS units. To address this issue, an adaptive coordinated optimization and dispatch method is proposed for a PV–BESS under strong PV power fluctuations. The method integrates rolling-horizon optimization, robust command decomposition, state-aware power allocation, and dynamic operating-limit feedback to coordinate plant-level dispatch objectives with unit-level operating capability. The main contributions are as follows:

(1) A robust decomposition method incorporating elastic-net regularization and abrupt-change protection is proposed for the total BESS control command. The command is decomposed into a low-frequency smooth component, a high-frequency dynamic component, and a sparse anomaly component. This allows occasional anomalies to be separated while preserving genuine rapid variations.
(2) A state-aware power allocation method is proposed for individual BESS units. Different command components are allocated according to the SOC and SOH of each

unit, while warning-state derating and fault isolation are incorporated to reduce the dynamic regulation burden on units with lower SOH.

(3) A closed-loop coordinated dispatch mechanism incorporating dynamic operating-limit feedback is developed. The available power and energy limits of the BESS are updated according to the states of individual units and fed back to the subsequent rolling-horizon optimization process, improving command executability under different operating conditions.

2. Modeling and Hierarchical Dispatch Framework for a PV–BESS

Highly variable weather conditions and differences in the operating states of individual BESS units pose considerable challenges to grid-connected power regulation, safe BESS operation, and coordinated control among the units. Accordingly, a hierarchical coordinated dispatch framework is developed for the PV–BESS to improve tracking of the grid power schedule and ensure safe BESS operation. As shown in Figure 1, the framework consists of a plant-level rolling optimization layer, a robust command decomposition layer, and a state-aware power allocation layer. The rolling optimization layer determines the total BESS control command based on PV power forecasts, the grid power schedule, and the BESS operating limits. The robust command decomposition layer further decomposes the total command into a low-frequency smooth component, a high-frequency dynamic component, and a sparse anomaly component. The state-aware power allocation layer assigns the different regulation components to individual energy storage units according to their SOC, SOH, and fault status. Following command execution, the SOC, fault status, and available power limits of each unit are updated. The aggregated BESS operating limits are then fed back to the rolling optimization layer to refine the feasible operating region for subsequent dispatch intervals. This process forms a closed-loop coordinated dispatch framework that proceeds from plant-level optimization to unit-level power allocation and then returns to plant-level optimization through state feedback.

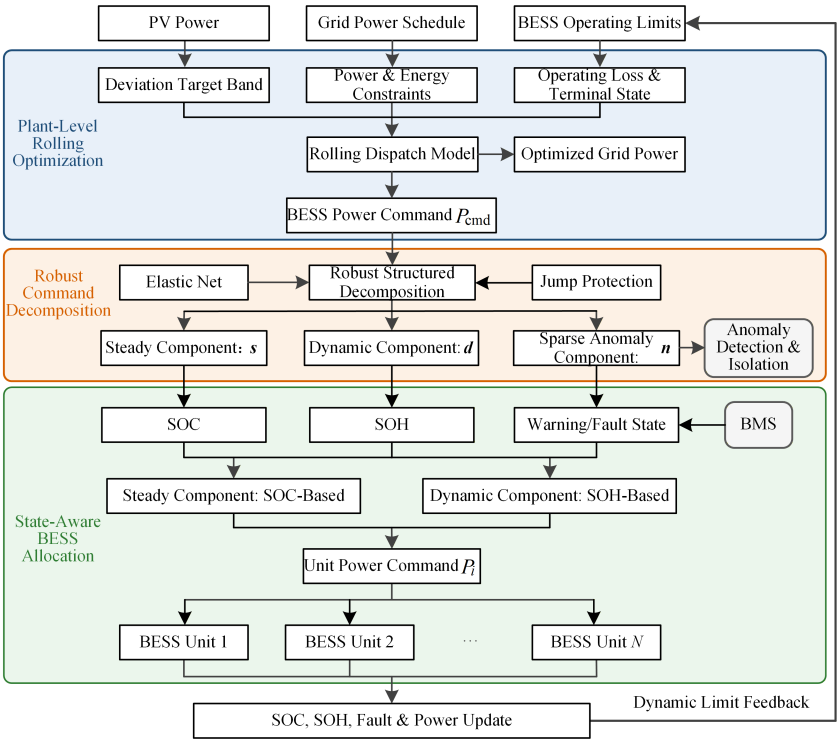


Figure 1. Hierarchical coordinated dispatch framework for the PV–BESS.

3. Rolling-Horizon Dispatch Optimization for a PV–BESS Considering Forecast Errors

Rolling-horizon optimization based on model predictive control continuously updates dispatch decisions using forecast information and system constraints [21]. To improve the adaptability of the PV–BESS to variations in PV power and BESS operating states, a rolling-horizon dispatch optimization model considering forecast errors is developed. The model uses PV power forecasts, the grid power schedule, and dynamic BESS operating limits as inputs. Over the prediction horizon, PV curtailment mitigation, tracking of the grid power schedule, battery degradation, and operating revenue are jointly considered to optimize the BESS charging and discharging power and grid-connected power. By updating the forecasts and BESS operating limits at each dispatch instant, the model adjusts subsequent dispatch decisions in response to variations in PV output and changes in BESS operating states.

3.1. Rolling-Horizon Optimization Objective Function

To balance PV curtailment mitigation, tracking of the grid power schedule, battery degradation, and operating revenue, a rolling-horizon optimization objective function is formulated. Let the current dispatch instant be t, the prediction horizon be N_p, and the dispatch interval be Δt. The overall objective function over the prediction horizon is expressed as

$$\min J = \sum_{k=1}^{N_p} \left[\lambda_1 F_{cur}(k) + \lambda_2 F_{dev}(k) + \lambda_3 F_{deg}(k) - \lambda_4 F_{pro}(k) \right], \tag{1}$$

where J denotes the total dispatch cost over the prediction horizon; $F_{cur}(k)$, $F_{dev}(k)$, $F_{deg}(k)$, and $F_{pro}(k)$ denote the PV curtailment penalty, grid-connection deviation penalty, battery degradation cost, and electricity sales revenue at interval k, respectively; and λ_1, λ_2, λ_3, and λ_4 are their corresponding weighting coefficients.

The PV curtailment penalty term $F_{cur}(k)$ is expressed as

$$F_{cur}(k) = M_{cur} P_{cur}(k) \Delta t, \tag{2}$$

where M_{cur} is the unit PV curtailment penalty coefficient, and $P_{cur}(k)$ is the curtailed PV power.

The grid-connection deviation penalty term $F_{dev}(k)$ is expressed as

$$F_{dev}(k) = c_{dev} \left[Z_{pos}^2(k) + Z_{neg}^2(k) \right] \Delta t, \tag{3}$$

where c_{dev} is the grid-connection deviation penalty coefficient. $Z_{pos}(k)$ and $Z_{neg}(k)$ denote the deviations of the grid-connected power above the upper limit and below the lower limit of the target band, respectively.

The battery degradation cost term $F_{deg}(k)$ is expressed as

$$F_{deg}(k) = c_{deg} [P_c(k) + P_d(k)] \Delta t, \tag{4}$$

where c_{deg} is the equivalent battery degradation cost coefficient, and $P_c(k)$ and $P_d(k)$ are the BESS charging and discharging power, respectively.

Equation (4) approximates battery cycling degradation based on the charging and discharging energy, where $[P_c(k) + P_d(k)]\Delta t$ represents the total charging and discharging energy during the k-th dispatch interval. For a battery of fixed capacity, greater cumulative charging and discharging energy corresponds to a larger number of equivalent full cycles

and, consequently, a higher degradation cost. This term is used to estimate the degradation cost in the rolling-horizon optimization rather than to directly predict the actual battery lifetime.

The electricity sales revenue term $F_{\mathrm{pro}}(k)$ is expressed as

$$F_{\mathrm{pro}}(k) = \pi_{\mathrm{TOU}}(k) P_{\mathrm{grid}}(k) \Delta t, \tag{5}$$

where $\pi_{\mathrm{TOU}}(k)$ is the time-of-use electricity price, and $P_{\mathrm{grid}}(k)$ is the grid-connected power.

3.2. BESS State Model Considering Dynamic Available Capacity

The operating state of the BESS during dispatch is primarily determined by its remaining dispatchable energy [22]. The current stored energy $E(k)$ is selected as the state variable to characterize the energy variation caused by battery charging and discharging. At each rolling dispatch instant t, the model updates the available capacity $E_{\mathrm{ava}}(t)$, initial stored energy, and charging and discharging power limits according to the current BESS operating state. The system SOC, denoted by $\mathrm{SOC}(k)$, is then calculated from $E(k)$ and $E_{\mathrm{ava}}(t)$. By updating these parameters and operating limits at each rolling step, variations in BESS health and available regulation capability are incorporated into the dispatch feasible region.

The stored-energy state transition is described by

$$E(k+1) = E(k) + \left[\eta_{\mathrm{c}} P_{\mathrm{c}}(k) - \frac{P_{\mathrm{d}}(k)}{\eta_{\mathrm{d}}} \right] \Delta t, \tag{6}$$

where k denotes the k-th dispatch interval within the current prediction horizon, $k = 1, 2, \ldots, N_{\mathrm{p}}$, and η_{c} and η_{d} are the charging and discharging efficiencies, respectively. The corresponding system-level SOC is calculated as

$$\mathrm{SOC}(k) = \frac{E(k)}{E_{\mathrm{ava}}(t)}, \tag{7}$$

where $E_{\mathrm{ava}}(t)$ is obtained by aggregating the current available capacities, health conditions, and fault states of the individual energy storage units and is treated as a known boundary parameter within the current rolling optimization horizon. At the next dispatch instant, this parameter is updated based on the latest state feedback.

3.3. Dynamic Feasible-Region Constraints

To ensure that the rolling-horizon optimization results comply with the actual operating capability of the BESS, the system-level operating limits obtained from BESS state assessment are incorporated into the upper-level optimization model. The stored energy of the BESS is subject to the following dynamic energy safety constraints:

$$\begin{aligned} & E_{\min}(t) \le E(k) \le E_{\max}(t) \\ & E_{\max}(t) = \mathrm{SOC}_{\max} E_{\mathrm{ava}}(t) \\ & E_{\min}(t) = \mathrm{SOC}^{\mathrm{d}}_{\min}(t) E_{\mathrm{ava}}(t), \end{aligned} \tag{8}$$

where $E_{\min}(t)$ and $E_{\max}(t)$ are the minimum and maximum available energy limits of the BESS obtained from state assessment at the current dispatch instant, respectively; $\mathrm{SOC}_{\max}$ is the maximum allowable SOC; and $\mathrm{SOC}^{\mathrm{d}}_{\min}(t)$ is the minimum allowable SOC at rolling dispatch instant t.

The BESS charging and discharging power constraints are given by

$$\begin{gathered} 0 \le P_{\mathrm{c}}(k) \le P_{\mathrm{c}}^{\max}(t) U_{\mathrm{c}}(k) \\ 0 \le P_{\mathrm{d}}(k) \le P_{\mathrm{d}}^{\max}(t) U_{\mathrm{d}}(k) \\ U_{\mathrm{c}}(k) + U_{\mathrm{d}}(k) \le 1, \qquad U_{\mathrm{c}}(k), U_{\mathrm{d}}(k) \in \{0,1\}, \end{gathered} \tag{9}$$

where $P_{\mathrm{c}}^{\max}(t)$ and $P_{\mathrm{d}}^{\max}(t)$ are the maximum allowable charging and discharging power of the BESS at the current dispatch instant, respectively; and $U_{\mathrm{c}}(k)$ and $U_{\mathrm{d}}(k)$ are the binary charging and discharging state variables, respectively.

The grid-connected power is constrained by

$$0 \le P_{\mathrm{grid}}(k) \le P_{\max}^{\mathrm{g}}, \tag{10}$$

where $P_{\max}^{\mathrm{g}}$ is the maximum power allowed by the grid-connection channel.

The nodal power balance of the PV–BESS is expressed as

$$P_{\mathrm{grid}}(k) = P_{\mathrm{PV}}(k) - P_{\mathrm{c}}(k) + P_{\mathrm{d}}(k) - P_{\mathrm{cur}}(k), \tag{11}$$

where $P_{\mathrm{PV}}(k)$ is the forecast PV power.

To avoid frequent BESS responses to minor deviations, the following target-band constraints are imposed on the tracking of the grid power schedule:

$$\begin{cases} P_{\mathrm{grid}}(k) - P_{\mathrm{plan}}(k) \le \varepsilon(k) + Z_{\mathrm{pos}}(k), \\ P_{\mathrm{plan}}(k) - P_{\mathrm{grid}}(k) \le \varepsilon(k) + Z_{\mathrm{neg}}(k), \\ Z_{\mathrm{pos}}(k) \ge 0, \quad Z_{\mathrm{neg}}(k) \ge 0. \\ \varepsilon(k) = \max\left\{\varepsilon_{\min}, \xi P_{\mathrm{plan}}(k)\right\}, \end{cases} \tag{12}$$

where $P_{\mathrm{plan}}(k)$ is the scheduled grid-connected power; $\varepsilon(k)$ is the allowable grid-connection deviation at the current dispatch interval; $\varepsilon_{\min}$ is the minimum allowable deviation-band width; and ξ is the allowable deviation ratio of the target band.

To enhance the recursive feasibility of rolling-horizon optimization and prevent excessive energy depletion near the end of the prediction horizon from adversely affecting subsequent dispatch, the following terminal energy constraint is imposed:

$$E(t + N_{\mathrm{p}}) \ge E_{\mathrm{T}}^{\min}(t), \tag{13}$$

where $E_{\mathrm{T}}^{\min}(t)$ is the minimum energy that must be retained at the end of the prediction horizon.

3.4. Rolling-Horizon Dispatch Procedure

At each rolling dispatch instant, an optimization problem is formulated over the prediction horizon using the latest PV power forecasts, grid power schedule, and system-level operating limits aggregated from the states of the individual energy storage units. Solving this problem yields an optimal control sequence for the next N_{p} dispatch intervals, of which only the control action for the current interval is implemented. After its implementation, the remaining energy and dynamic operating limits of the BESS are updated according to the actual operating results. The optimization problem is then reformulated and solved at the next dispatch instant.

The total BESS control command represents the overall power regulation demand determined by the rolling optimization layer and serves as the input to the subsequent command decomposition model. It is defined as

$$P_{\mathrm{cmd}}(k) = P_{\mathrm{BESS}}(k) = P_{\mathrm{d}}(k) - P_{\mathrm{c}}(k), \tag{14}$$

where $P_{\mathrm{cmd}}(k)$ is the total power command issued to the BESS at interval k. A positive value, $P_{\mathrm{cmd}}(k) > 0$, indicates BESS discharging, whereas a negative value, $P_{\mathrm{cmd}}(k) < 0$, indicates BESS charging. $P_{\mathrm{BESS}}(k)$ denotes the net charging/discharging power of the BESS.

4. Robust Locally Smooth Decomposition with Elastic-Net Regularization

The total BESS control command $P_{\mathrm{cmd}}(k)$ obtained from the rolling optimization model represents the overall power regulation demand of the PV–BESS. It comprises slowly varying energy regulation demand, dynamic regulation demand caused by rapid PV power fluctuations, and noise or local anomalies. Directly allocating this command to individual energy storage units may result in improper power allocation among units with different health conditions and increase cycling degradation due to frequent charging and discharging. Therefore, a robust command decomposition model is developed to separate the total command into a smooth regulation component, a dynamic regulation component, and a sparse anomaly component. While maintaining energy consistency with the total command, the model provides differentiated command inputs for the subsequent state-aware power allocation of individual energy storage units.

4.1. Decomposition of the Total Control Command

Let $\mathbf{P}_{\mathrm{cmd}}$ denote the output sequence of the total BESS control command. Considering the effects of forecast errors, noise, and anomalous disturbances during actual operation, the command sequence input to the robust decomposition model is expressed as

$$\widetilde{\mathbf{P}}_{\mathrm{cmd}} = \mathbf{s} + \mathbf{d} + \mathbf{n} + \mathbf{r}, \tag{15}$$

where $\mathbf{s}$ is the smooth regulation component representing the sustained regulation demand of the BESS; $\mathbf{d}$ is the dynamic regulation component representing the power regulation demand caused by rapid PV power variations; $\mathbf{n}$ is the sparse anomaly component describing impulsive disturbances or local outliers; and $\mathbf{r}$ is the residual component representing small random disturbances not captured by the other components.

The structured command used for lower-level execution and power allocation is defined as

$$\mathbf{q} = \mathbf{s} + \mathbf{d}, \tag{16}$$

where $\mathbf{q}$ is the effective execution command used for power allocation among individual energy storage units. It retains the effective regulation demand contained in the total control command while excluding the sparse anomaly and residual components, thereby reducing the influence of anomalies on lower-level BESS power allocation.

4.2. Robust Decomposition Optimization Model

To effectively separate the different variation characteristics of the total control command, difference regularization is employed to characterize the temporal behavior of each component. Specifically, a second-order difference penalty is used to suppress fluctuations in the smooth component, whereas a first-order difference penalty is applied to characterize variations in the dynamic component. Because the dynamic component must preserve rapid variations while maintaining decomposition stability, an elastic-net regularization term is further introduced [23]. This term combines an L_1 sparsity penalty with an L_2

magnitude penalty to balance dynamic-feature extraction and decomposition stability. In addition, an abrupt-change protection mechanism is incorporated to prevent genuine abrupt changes in the total command from being excessively smoothed or misclassified as anomalies.

First, the variation in the total control command between two consecutive intervals is calculated as

$$\Delta P_{\mathrm{cmd}}(k) = P_{\mathrm{cmd}}(k+1) - P_{\mathrm{cmd}}(k), \tag{17}$$

When $|\Delta P_{\mathrm{cmd}}(k)| \geq \delta_J$, the corresponding position is identified as an abrupt-change edge and included in the edge set $\mathcal{J}_{\mathrm{e}}$, where δ_J is the abrupt-change detection threshold. Based on the detected edges and their neighboring samples, the protection weight matrices $\mathbf{W}_{\mathrm{d}}$ and $\mathbf{W}_{\mathrm{n}}$ are constructed for the dynamic and anomaly components, respectively. The robust decomposition model is then formulated as

$$\begin{aligned} &\min_{\mathbf{s},\mathbf{d},\mathbf{n}} \frac{1}{2}\left\|\widetilde{\mathbf{P}}_{\mathrm{cmd}} - \mathbf{s} - \mathbf{d} - \mathbf{n}\right\|_2^2 + \mu_1\|\mathbf{D}_2\mathbf{s}\|_2^2 + \\ &\mu_2\|\mathbf{W}_{\mathrm{d}}\mathbf{D}_1\mathbf{d}\|_2^2 + \mu_3\|\mathbf{W}_{\mathrm{n}}\mathbf{n}\|_1 + \mu_4\left[\alpha\|\mathbf{d}\|_1 + (1-\alpha)\|\mathbf{d}\|_2^2\right], \end{aligned} \tag{18}$$

where μ_1, μ_2, μ_3, and μ_4 are the regularization weights. The first term is the data-fidelity term, which ensures that the components reconstruct the original total control command while retaining small random disturbances in the reconstruction residual. The second term imposes a second-order difference penalty on the smooth component, where $\mathbf{D}_2$ is the second-order difference matrix. The third term applies a weighted first-order difference penalty to the dynamic component, where $\mathbf{D}_1$ is the first-order difference matrix. The fourth term uses a weighted L_1-norm penalty to extract the sparse anomaly component. The fifth term is the elastic-net regularization term, where $\alpha \in [0,1]$ is the elastic-net mixing parameter. By combining the L_1 sparsity penalty and the squared L_2 magnitude penalty, this term balances dynamic-feature extraction and decomposition stability.

The protection weights for the dynamic and anomaly components are defined as

$$\begin{aligned} w_{\mathrm{d}}(k) &= \begin{cases} \bar{w}_{\mathrm{d}}, & k \in \mathcal{J}_{\mathrm{e}} \\ 1, & k \notin \mathcal{J}_{\mathrm{e}} \end{cases}, \quad 0 < \bar{w}_{\mathrm{d}} < 1 \\ w_{\mathrm{n}}(k) &= \begin{cases} \bar{w}_{\mathrm{n}}, & k \in \mathcal{J}_{\mathrm{s}} \\ 1, & k \notin \mathcal{J}_{\mathrm{s}} \end{cases}, \quad \bar{w}_{\mathrm{n}} > 1, \end{aligned} \tag{19}$$

where $\mathcal{J}_{\mathrm{s}}$ is the set of protected samples determined from the abrupt-change edges and their neighboring positions. The parameters $\bar{w}_{\mathrm{d}}$ and $\bar{w}_{\mathrm{n}}$ are the protection coefficients for the dynamic and anomaly components, respectively. A smaller $\bar{w}_{\mathrm{d}}$ reduces the first-order difference penalty on the dynamic component at genuine abrupt-change positions, whereas a larger $\bar{w}_{\mathrm{n}}$ prevents these changes from being assigned to the sparse anomaly component.

To prevent the dynamic regulation component from altering the mean power and energy baseline of the total command, the following zero-mean constraint is imposed:

$$\sum_{k=1}^{K} d(k) = 0, \tag{20}$$

where K is the length of the total control command sequence.

4.3. ADMM-Based Solution Procedure

The proposed decomposition model contains quadratic difference-regularization terms, sparse regularization terms, and executable-command constraints. Because the variables are coupled through data reconstruction, solving the model directly is difficult.

Therefore, the alternating direction method of multipliers (ADMM) is adopted to separate the regularization terms and constraints into tractable subproblems [24].

Auxiliary variables $\mathbf{z}_{\mathrm{d}}$, $\mathbf{z}_{\mathrm{n}}$, and $\mathbf{q}$ are introduced to decouple the L_1-norm regularization of the dynamic component, the weighted L_1-norm regularization of the anomaly component, and the executable-command constraint, respectively. They satisfy

$$\mathbf{d} = \mathbf{z}_{\mathrm{d}}, \qquad \mathbf{n} = \mathbf{z}_{\mathrm{n}}, \qquad \mathbf{s} + \mathbf{d} = \mathbf{q}, \qquad \mathbf{q} \in \Omega, \tag{21}$$

where Ω denotes the set of executable BESS commands.

Through this variable splitting, the original problem is decomposed into several subproblems involving quadratic optimization, soft-thresholding operations, and projection onto the executable-command set. At iteration $r+1$, the primary variables $\mathbf{s}$, $\mathbf{d}$, and $\mathbf{n}$ are first updated while the auxiliary and scaled dual variables are fixed. This update corresponds to a convex quadratic subproblem with quadratic regularization and can be obtained by solving a system of linear equations.

After updating the primary variables, the sparse auxiliary variables associated with the dynamic and anomaly components are updated using the soft-thresholding operator:

$$\begin{aligned} \mathbf{z}_{\mathrm{d}}^{r+1} &= \mathcal{S}_{\mu_4 \alpha/\rho}(\mathbf{d}^{r+1} + \mathbf{u}_{\mathrm{d}}^{r}) \\ \mathbf{z}_{\mathrm{n}}^{r+1} &= \mathcal{S}_{(\mu_3/\rho)\mathbf{w}_{\mathrm{n}}}\left(\mathbf{n}^{r+1} + \mathbf{u}_{\mathrm{n}}^{r}\right), \end{aligned} \tag{22}$$

where r is the iteration index, ρ is the ADMM penalty parameter, and $\mathbf{u}_{\mathrm{d}}$ and $\mathbf{u}_{\mathrm{n}}$ are the corresponding scaled dual variables. The operator $\mathcal{S}_{\tau}(\cdot)$ denotes the soft-thresholding operator with threshold τ.

The sum of the smooth and dynamic components is subsequently projected onto the executable-command set Ω:

$$\mathbf{q}^{r+1} = \Pi_{\Omega}(\mathbf{s}^{r+1} + \mathbf{d}^{r+1} + \mathbf{u}_{\mathrm{q}}^{r}), \tag{23}$$

where $\Pi_{\Omega}(\cdot)$ denotes the projection onto Ω, and $\mathbf{u}_{\mathrm{q}}$ is the scaled dual variable associated with the structured-command consistency constraint. The set Ω incorporates the BESS power limits, charging/discharging direction consistency, and consistency between the mean power of the structured command and that of the upper-level total control command, thereby ensuring that the decomposition results are physically executable.

Finally, the scaled dual variables are updated as

$$\begin{aligned} \mathbf{u}_{\mathrm{d}}^{r+1} &= \mathbf{u}_{\mathrm{d}}^{r} + \mathbf{d}^{r+1} - \mathbf{z}_{\mathrm{d}}^{r+1} \\ \mathbf{u}_{\mathrm{n}}^{r+1} &= \mathbf{u}_{\mathrm{n}}^{r} + \mathbf{n}^{r+1} - \mathbf{z}_{\mathrm{n}}^{r+1} \\ \mathbf{u}_{\mathrm{q}}^{r+1} &= \mathbf{u}_{\mathrm{q}}^{r} + \mathbf{s}^{r+1} + \mathbf{d}^{r+1} - \mathbf{q}^{r+1}, \end{aligned} \tag{24}$$

The iterative procedure terminates when both the primal and dual residuals fall below their prescribed tolerances. Upon convergence, $\mathbf{s} + \mathbf{d}$ constitutes the executable BESS command, whereas the sparse anomaly component $\mathbf{n}$ is used for anomaly detection and isolation. The smooth component $\mathbf{s}$ and dynamic component $\mathbf{d}$ are then passed to the state-aware power allocation model for individual energy storage units.

5. Unit-Level Power Allocation Model Considering State Differences Among Energy Storage Units

To address internal power allocation within the BESS, a state-aware power allocation model is developed to account for differences in the SOC, SOH, and fault status of individual energy storage units. The smooth and dynamic regulation components obtained

in Section 3 are allocated separately according to these state differences. Specifically, the dynamic component is preferentially assigned to units with higher SOH, whereas the smooth component is allocated according to the charging or discharging SOC margin of each unit. Following the initial allocation, the power commands are corrected subject to unit-level power limits and SOC constraints to ensure their executability. Finally, the available power and energy limits of the individual units are aggregated and fed back to the upper-level rolling optimization model to update the BESS operating limits for subsequent dispatch intervals.

5.1. State-Aware Differentiated Power Allocation

Following robust decomposition, the structured executable command of the BESS is given by

$$q(k) = s(k) + d(k), \tag{25}$$

where $s(k)$ and $d(k)$ are the smooth and dynamic components, respectively.

To allocate this command among the equivalent energy storage units within the BESS, a state-aware power allocation method is developed by jointly considering the SOC, SOH, and operating status of each unit.

Assume that the BESS comprises N equivalent energy storage units. The states of unit i at interval k are denoted by $\mathrm{SOC}_i(k)$, $\mathrm{SOH}_i(k)$, and $\mathrm{St}_i(k)$. Here, $\mathrm{St}_i(k) \in \{0,1,2\}$ represents the normal, warning, and fault states, respectively. To characterize the ability of each unit to participate in power allocation under different operating states, an availability indicator $\omega_i(k)$ and an operating derating factor $\gamma_i(k)$ are introduced:

$$\begin{aligned} \omega_i(k) &= \begin{cases} 1, & \mathrm{St}_i(k) < 2 \\ 0, & \mathrm{St}_i(k) = 2. \end{cases} \\ \gamma_i(k) &= \begin{cases} 1, & \mathrm{St}_i(k) = 0 \\ \gamma_{\mathrm{w}}, & \mathrm{St}_i(k) = 1, \\ 0, & \mathrm{St}_i(k) = 2. \end{cases} \end{aligned} \tag{26}$$

where $\gamma_{\mathrm{w}} \in (0,1)$ is the warning-state derating factor. Faulted units are excluded from power allocation, whereas units in the warning state participate according to their derated regulation capabilities.

Because the dynamic component varies frequently and has a considerable effect on battery cycling degradation, its allocation weights are determined according to SOH:

$$W_i^{\mathrm{H}}(k) = \frac{\omega_i(k)\gamma_i(k)[\max(0, \mathrm{SOH}_i(k) - \mathrm{SOH}_{\min})]^{\beta}}{\sum_{j=1}^{N} \omega_j(k)\gamma_j(k)\left[\max\left(0, \mathrm{SOH}_j(k) - \mathrm{SOH}_{\min}\right)\right]^{\beta}}, \tag{27}$$

where $\mathrm{SOH}_{\min}$ is the minimum health threshold, and β is the SOH sensitivity coefficient.

The smooth component primarily represents sustained energy regulation demand and is therefore allocated according to the available SOC regulation margin of each unit. With discharging power defined as positive and charging power as negative, the low-frequency regulation margin is defined as

$$M_i^{\mathrm{L}}(k) = \begin{cases} \max\{0, \mathrm{SOC}_{\max} - \mathrm{SOC}_i(k)\}, & s(k) < 0, \\ \max\left\{0, \mathrm{SOC}_i(k) - \mathrm{SOC}_{\min}^{\mathrm{d}}\right\}, & s(k) > 0, \\ 0, & s(k) = 0. \end{cases} \tag{28}$$

Accordingly, the allocation weight of the smooth component is given by

$$W_i^{\mathrm{L}}(k) = \frac{\omega_i(k)\gamma_i(k)M_i^{\mathrm{L}}(k)}{\sum_{j=1}^{N}\omega_j(k)\gamma_j(k)M_j^{\mathrm{L}}(k)}, \tag{29}$$

Based on the dynamic- and smooth-component allocation weights, the initial power command assigned to unit i is

$$P_i^0(k) = W_i^{\mathrm{H}}(k)d(k) + W_i^{\mathrm{L}}(k)s(k), \tag{30}$$

5.2. Unit-Level Power Allocation and Constraint Correction

The initial power command $P_i^0(k)$ obtained from state-aware allocation may be restricted by the unit-level power limits, available SOC margin, warning-state derating, and fault isolation. Therefore, the allocated power commands are corrected while retaining the initial allocation pattern as closely as possible, such that the final executable power satisfies the physical constraints and remains close to the initial commands.

First, the total executable power of the BESS is determined from the currently available charging and discharging power limits of all energy storage units:

$$P_{\mathrm{exe}}(k) = \min\{\max[q(k), -P_{\mathrm{c}}^{\max}(k)], P_{\mathrm{d}}^{\max}(k)\}, \tag{31}$$

When sufficient regulation capability is available, $q(k)$ lies within the current regulation range, and thus

$$P_{\mathrm{exe}}(k) = q(k), \tag{32}$$

When the regulation capability is restricted by SOC limits, warning-state derating, or fault isolation, $q(k)$ is clipped to the currently available BESS power limits. The unit-level power commands are then corrected by solving the following optimization problem:

$$\begin{aligned} &\min_{P_i(k)} \sum_{i=1}^{N}\left[P_i(k) - P_i^0(k)\right]^2 \\ &\text{s.t.} \sum_{i=1}^{N} P_i(k) = P_{\mathrm{exe}}(k) \\ &-P_{i,\mathrm{c}}^{\max}(k) \le P_i(k) \le P_{i,\mathrm{d}}^{\max}(k) \\ &\mathrm{SOC}_{\min}^{\mathrm{d}}(k) \le \mathrm{SOC}_i(k+1) \le \mathrm{SOC}_{\max}, \end{aligned} \tag{33}$$

where $P_i(k)$ is the corrected power command executed by unit i, and $P_{i,\mathrm{c}}^{\max}(k)$ and $P_{i,\mathrm{d}}^{\max}(k)$ are the maximum available charging and discharging power of unit i under its current operating state, respectively.

5.3. State Update and Dynamic Operating-Limit Feedback

After power allocation, the SOC of each energy storage unit is updated according to its actual executed power. With $P_i(k) > 0$ denoting discharging and $P_i(k) < 0$ denoting charging, the discharging and charging power components are defined as

$$\begin{aligned} P_i^+(k) &= \max\{P_i(k), 0\} \\ P_i^-(k) &= \max\{-P_i(k), 0\}, \end{aligned} \tag{34}$$

The SOC of unit i is then updated as

$$\mathrm{SOC}_i(k+1) = \mathrm{SOC}_i(k) - \frac{P_i^+(k)\Delta t}{\eta_{\mathrm{d}}E_i\mathrm{SOH}_i(k)} + \frac{\eta_{\mathrm{c}}P_i^-(k)\Delta t}{E_i\mathrm{SOH}_i(k)}, \tag{35}$$

where E_i is the rated energy capacity of unit i.

To feed the lower-level unit states back to the upper-level rolling optimization model and ensure that the dispatch limits reflect the actual regulation capability of the BESS, system-level equivalent states are constructed. Considering the health conditions and fault-isolation states of the individual units, the current equivalent stored energy of the BESS is defined as

$$E(k) = \sum_{i=1}^{N} \mathrm{SOC}_i(k) E_i \mathrm{SOH}_i(k) \omega_i(k), \tag{36}$$

The currently available BESS capacity is defined as

$$E_{\mathrm{ava}}(k) = \sum_{i=1}^{N} E_i \mathrm{SOH}_i(k) \omega_i(k), \tag{37}$$

Accordingly, the equivalent system-level SOC is given by

$$\mathrm{SOC}(k) = \frac{E(k)}{E_{\mathrm{ava}}(k)}, \tag{38}$$

To reduce the risk of deep discharge in aged energy storage units, the lower SOC limit is dynamically adjusted according to the overall health condition of the BESS. The equivalent system-level SOH is defined as

$$\mathrm{SOH}(k) = \frac{\sum_{i=1}^{N} E_i \mathrm{SOH}_i(k) \omega_i(k)}{\sum_{i=1}^{N} E_i \omega_i(k)}, \tag{39}$$

The corresponding dynamic lower SOC limit is expressed as

$$\mathrm{SOC}_{\min}^{\mathrm{d}}(k) = \mathrm{SOC}_{\min} + \beta_{\mathrm{soc}}[1 - \mathrm{SOH}(k)], \tag{40}$$

where $\mathrm{SOC}_{\min}$ is the baseline lower SOC limit, and β_{soc} is the aging-protection coefficient.

Furthermore, the maximum charging and discharging power limits used by the upper-level optimization model are obtained by aggregating the currently available power limits of the individual energy storage units:

$$\begin{aligned} P_{\mathrm{c}}^{\max}(k) &= \sum_{i=1}^{N} P_{i,\mathrm{c}}^{\max}(k) \\ P_{\mathrm{d}}^{\max}(k) &= \sum_{i=1}^{N} P_{i,\mathrm{d}}^{\max}(k), \end{aligned} \tag{41}$$

In summary, the proposed power allocation method accounts for differences in SOH, SOC margin, and fault status among individual energy storage units. By aggregating the unit-level operating states into system-level available operating limits and feeding them back to the upper-level rolling optimization model, the dispatch model can continuously adapt to variations in the actual regulation capability of the BESS. This feedback improves the executability of the PV–BESS coordinated dispatch commands and enhances the operational safety of the BESS.

6. Case Study and Results Analysis

Actual operating data collected in 2023 from a 130 MW PV power plant in a high-altitude region of Xinjiang, China, are used for the case study. The sampling interval is

5 min, resulting in 288 data points per day. Based on previous optimal sizing results, the rated power and rated energy capacity of the BESS are set to 10.6 MW and 33.8 MWh, respectively. The PV–BESS simulation model is implemented in MATLAB R2024a (The MathWorks, Inc., Natick, MA, USA), and its structure and information flow are shown in Figure 2. The main simulation parameters are listed in Table 2.

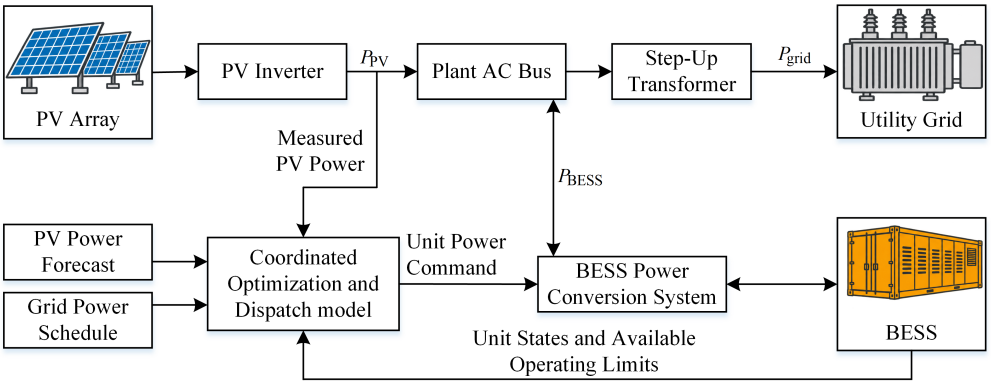


Figure 2. Simulation structure and information flow of the PV–BESS.

Table 2. Main simulation parameters.

Parameter	Symbol	Value	Parameter	Symbol	Value
Dispatch interval	Δt	5 min	ADMM penalty parameter	ρ	0.5
Prediction horizon	N_p	24 steps (2 h)	Dynamic protection coefficient	$\bar{w}_d$	0.2
Charging/discharging efficiency	η_c, η_d	0.95	Anomaly protection coefficient	$\bar{w}_n$	5
Target-band ratio	ξ	15%	Minimum SOH threshold	SOH_{min}	0.8
Objective-function weights	$\lambda_1, \lambda_2, \lambda_3, \lambda_4$	200, 150, 50, 1	SOH sensitivity coefficient	β	2
Decomposition regularization weights	$\mu_1, \mu_2, \mu_3, \mu_4$	0.25, 0.055, 0.015, 0.008	Dynamic lower-SOC-limit coefficient	β_{soc}	0.2
Elastic-net mixing parameter	α	0.3	Warning-state derating factor	γ_w	0.5
TOU tariff (deep-valley period)	$\pi_{TOU}(k)$	0.023 CNY/kWh	TOU tariff (valley period)	$\pi_{TOU}(k)$	0.0575 CNY/kWh
TOU tariff (flat period)	$\pi_{TOU}(k)$	0.23 CNY/kWh	TOU tariff (peak period)	$\pi_{TOU}(k)$	0.4025 CNY/kWh
TOU tariff (critical-peak period)	$\pi_{TOU}(k)$	0.46 CNY/kWh			

6.1. Selection and Characterization of Typical Operating Conditions

Based on the full-year actual and forecast PV power data at a 5-min resolution, daily energy generation, forecast root mean square error (RMSE), intraday cumulative fluctuation, and maximum ramp rate are selected as characteristic indicators. The intraday cumulative fluctuation is calculated as the sum of the absolute power changes between consecutive sampling points, while the maximum ramp rate is defined as the maximum power change per unit time between consecutive sampling points. After normalization, the four indicators are combined using a multi-criteria composite scoring method to select four typical operating conditions, denoted as TD1–TD4. Their normalized characteristics are compared in Figure 3.

As shown in Figure 3, TD1 exhibits relatively high PV output with small fluctuations and is therefore characterized by high output and low variability. TD2 has a relatively low intraday output level. TD3 has the largest cumulative fluctuation, accompanied by relatively high forecast errors and ramp rates, indicating sustained strong fluctuations. In contrast, TD4 exhibits more pronounced local abrupt power changes and ramping behavior. Because TD3 simultaneously captures the effects of continuous PV power fluctuations and forecast errors on BESS dispatch, it is selected as the primary operating condition for the subsequent analysis. Its PV power profiles and grid power schedule are shown in Figure 4.

Under this condition, the actual PV power frequently deviates from both the forecast power and the grid power schedule during the main generation period, providing a representative case for evaluating the proposed method in terms of forecast-error compensation, total command decomposition, and BESS power allocation.

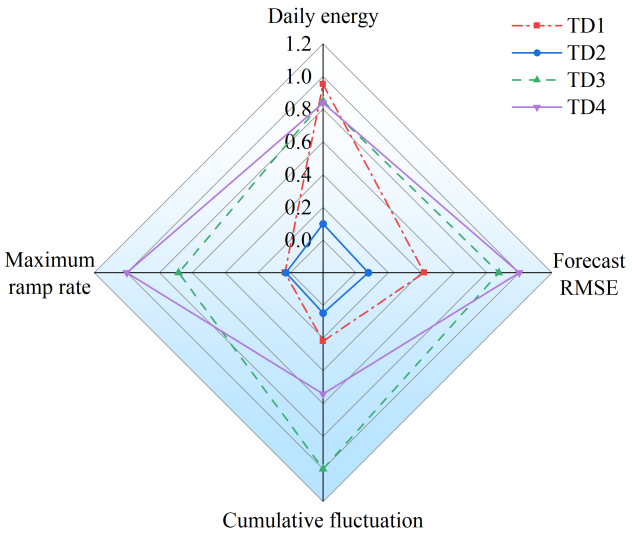


Figure 3. Comparison of normalized characteristics among four typical days.

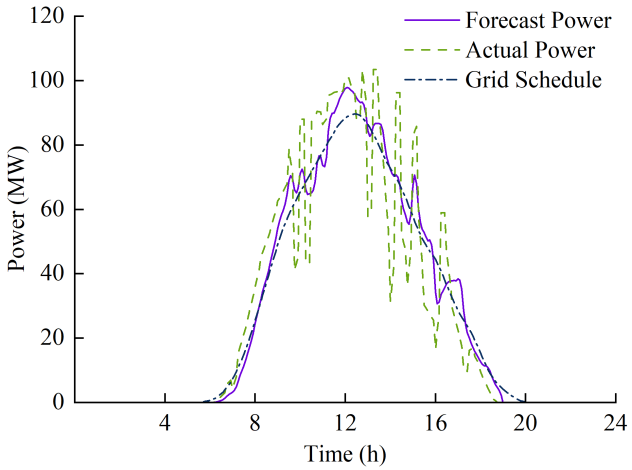


Figure 4. PV power profiles and grid power schedule on the typical day with strong fluctuations.

6.2. Analysis of PV–BESS Rolling-Horizon Dispatch Results

To evaluate the power regulation capability of the proposed PV–BESS rolling-horizon dispatch model, simulations are conducted using the selected typical day characterized by strong PV power fluctuations. The forecast and actual PV power, grid power schedule, and optimized grid-connected power are shown in Figure 5. As illustrated, the actual PV output fluctuates considerably during the main generation period and frequently deviates from both the forecast power and the grid power schedule. In response to variations in PV output and the current BESS operating state, the rolling optimization model adjusts the BESS charging and discharging power in real time, bringing the optimized grid-connected power closer to the grid power schedule and mitigating the impact of PV forecast errors on grid-connected power stability. During the simulation, the BESS charging and discharging power remains within its rated power of 10.6 MW, while the SOC remains between 0.45 and 0.88. The terminal SOC at the end of the prediction horizon is 0.45. These results satisfy the BESS power, energy, and terminal-state constraints, demonstrating the executability of the rolling-horizon dispatch results.

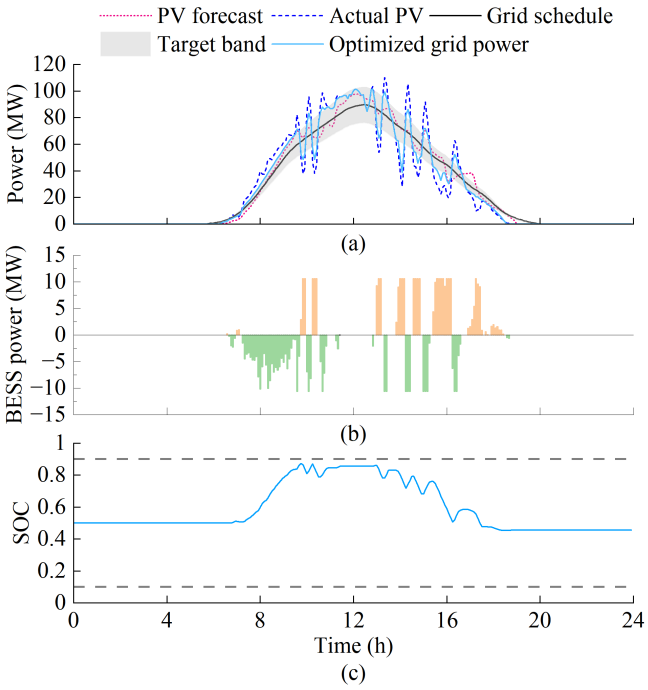


Figure 5. Rolling-horizon dispatch results of the PV–BESS. (**a**) PV output and dispatch schedule curves; (**b**) BESS power, with orange indicating discharging and green indicating charging; (**c**) BESS SOC.

Figure 6 presents the curtailed PV power and the out-of-band deviations, with the no-BESS scenario serving as the operating baseline. With the BESS participating in dispatch, the RMSE of the out-of-band deviation decreases from 6.486 MW in the no-BESS scenario to 2.453 MW, corresponding to a reduction of 62.18%. This result indicates that the total BESS control command effectively compensates for PV forecast errors and reduces both positive and negative deviations beyond the target band. The curtailed PV energy on the typical day is 1.647 MWh, and the PV utilization rate reaches 99.741%. PV curtailment occurs mainly during periods of high PV output when BESS charging capability is limited. The small out-of-band deviations during low-output periods are primarily caused by insufficient PV generation and limited BESS discharging capability. Overall, the rolling optimization model effectively improves tracking of the grid power schedule while satisfying BESS operating constraints and maintaining a high level of PV utilization.

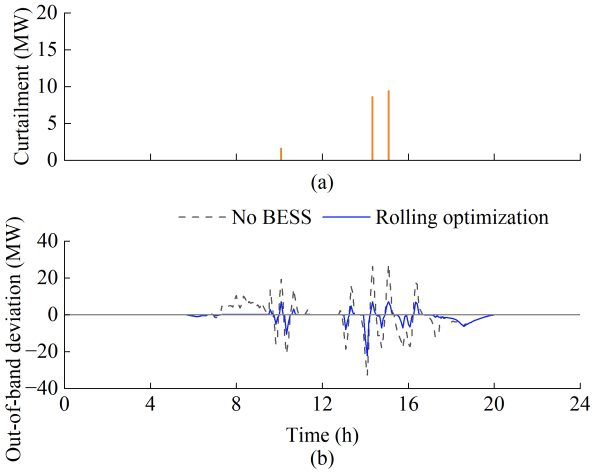


Figure 6. PV curtailment and out-of-band deviations. (**a**) PV curtailment power; (**b**) Out-of-band deviations with and without BESS.

6.3. Analysis of Robust Total Command Decomposition Results

To evaluate the ability of the proposed method to decompose the total BESS control command, the command obtained for the typical strong-fluctuation day is used as the input and decomposed into a low-frequency smooth component, a high-frequency dynamic component, and a sparse anomaly component. The low- and high-frequency components jointly constitute the executable command, whereas the sparse anomaly component represents occasional data anomalies and is excluded from subsequent BESS power allocation. The decomposition results are shown in Figure 7.

The executable command generally preserves the variation trend of the observed command. The low-frequency component captures the sustained power regulation demand, while the high-frequency component retains rapid power variations. The sparse anomaly component responds only at a few anomalous instants. These results demonstrate that the proposed method effectively separates the low-frequency smooth demand from the high-frequency dynamic demand while reducing the influence of occasional anomalies on subsequent power allocation.

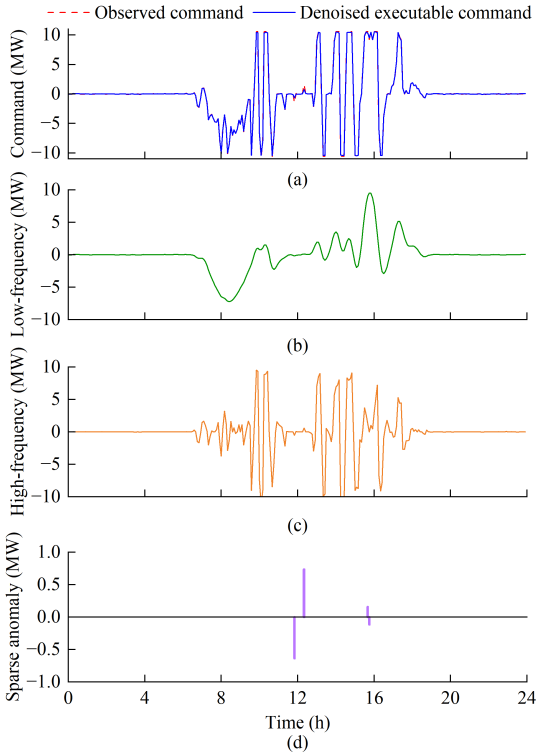


Figure 7. Robust decomposition results of the total BESS control command. (**a**) Observed and denoised executable commands; (**b**) Low-frequency component; (**c**) High-frequency component; (**d**) Sparse anomaly component.

To investigate the effects of elastic-net regularization and the abrupt-change protection mechanism, three variants are evaluated: the complete model, the model without elastic-net regularization, and the model without abrupt-change protection. Ten independent trials are conducted for each variant. The high-frequency-component RMSE, high-frequency correlation coefficient, and strong-fluctuation preservation rate are used as evaluation metrics. Table 3 reports the mean and standard deviation of each metric.

For the complete model, the high-frequency-component RMSE is 0.671 MW, and the correlation coefficient reaches 0.983. After removing elastic-net regularization, the RMSE increases to 2.015 MW and the correlation coefficient decreases to 0.881, demonstrating that elastic-net regularization improves the extraction accuracy of the high-frequency

component. Without abrupt-change protection, the strong-fluctuation preservation rate decreases from 97.36% to 30.99%, indicating that conventional smoothing constraints may excessively smooth genuine rapid variations or misclassify them as anomalies.

Table 3. Ablation study results for different model configurations.

Model Configuration	High-Frequency-Component RMSE (MW)	High-Frequency Correlation Coefficient	Command Fluctuation Retention Rate (%)
Complete model	0.671 ± 0.012	0.983 ± 0.001	97.361 ± 0.108
Without elastic-net regularization	2.015 ± 0.042	0.881 ± 0.005	98.379 ± 0.090
Without abrupt-change protection	2.197 ± 0.001	0.815 ± 0.002	30.995 ± 0.073

Figure 8 further presents a local comparison over a strong-fluctuation interval. The output of the complete model closely matches the clean reference command and preserves its rapid rising and falling transitions. In contrast, the model without abrupt-change protection exhibits considerable amplitude attenuation and waveform smoothing. These results demonstrate that the abrupt-change protection mechanism reduces the distortion of genuine dynamic variations during decomposition.

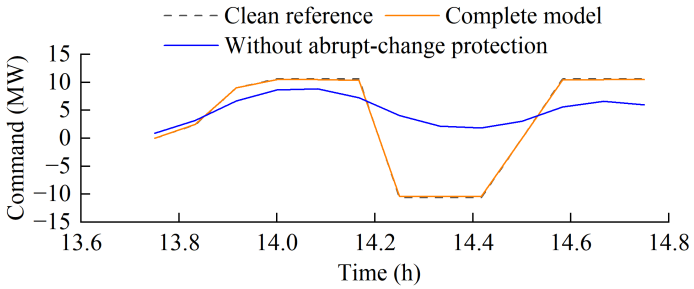


Figure 8. Local decomposition results over a strong-fluctuation interval.

To further evaluate the proposed method against commonly used decomposition methods, wavelet transform (WT), variational mode decomposition (VMD), and local mean decomposition (LMD) are selected for comparison. All methods use the same input command and evaluation metrics, and the results are presented in Table 4. The proposed method achieves lower RMSE values for both the low- and high-frequency components, a higher correlation coefficient for the high-frequency component, and a higher retention rate for high-frequency fluctuations. These results indicate that elastic-net regularization and abrupt-change protection can suppress the influence of anomalies while preserving genuine high-frequency regulation demand, thereby providing accurate control inputs for subsequent state-aware power allocation.

Table 4. Performance comparison of total-control-command decomposition methods.

Method	Low-Frequency RMSE (MW)	High-Frequency Correlation Coefficient	High-Frequency RMSE (MW)	High-Frequency Fluctuation Retention Rate (%)
Proposed method	0.712 ± 0.007	0.9831 ± 0.0005	0.671 ± 0.012	87.086 ± 0.286
WT	1.118 ± 0.001	0.9562 ± 0.0006	1.147 ± 0.005	69.814 ± 0.351
VMD	1.009 ± 0.093	0.9422 ± 0.0050	0.993 ± 0.068	50.685 ± 1.950
LMD	1.858 ± 0.362	0.8182 ± 0.0719	1.956 ± 0.337	63.622 ± 5.962

6.4. Validation of State-Aware Power Allocation and Dynamic Operating-Limit Feedback

6.4.1. Analysis of State-Aware Power Allocation Results

To validate the differentiated allocation of high- and low-frequency power commands, the BESS is divided into ten equivalent units with a total rated power of 10.6 MW and a total rated energy capacity of 33.8 MWh. Different initial SOC and SOH values are assigned to the units. The high-frequency component is allocated according to SOH, whereas the low-frequency component is allocated according to the available charging or discharging SOC margin.

Figure 9 presents the allocation results for the high-frequency component. The high-frequency regulation energy assigned to each unit generally decreases with decreasing SOH. Units with higher SOH undertake more high-frequency regulation, indicating that such tasks are preferentially assigned to healthier units.

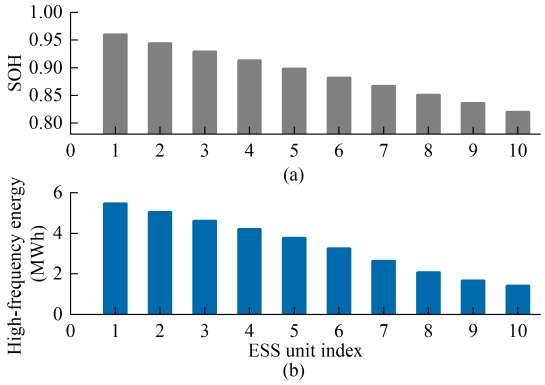


Figure 9. High-frequency power allocation among energy storage units with different SOH values. (**a**) SOH of individual units; (**b**) High-frequency regulation energy assigned to each unit.

Figure 10 illustrates the relationships between the SOC margin and low-frequency power under charging and discharging conditions. During charging, units with greater remaining charging margins undertake more charging power. During discharging, units farther from the lower SOC limit undertake more discharging power. The scatter plots show that the low-frequency power assigned to each unit increases with its SOC margin in the corresponding direction, confirming that the proposed strategy allocates low-frequency power according to differences in unit SOC.

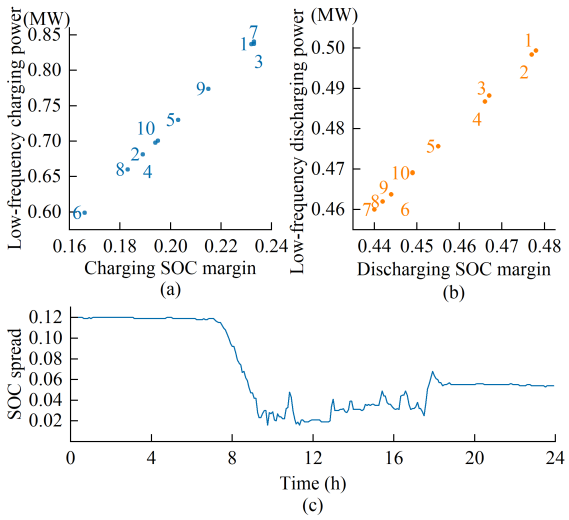


Figure 10. State-aware allocation of the low-frequency component. (**a**) Unit low-frequency charging power versus SOC margin; (**b**) Unit low-frequency discharging power versus SOC margin; (**c**) SOC spread over time.

To further assess the effect of differentiated allocation of high- and low-frequency power commands, a long-term comparative degradation analysis is conducted considering SOH evolution and available-capacity feedback. The comparison includes proportional allocation, SOC-margin-based allocation, the health-aware rule-based method proposed by Fan et al. [16], the dynamic-feedback equalization method proposed by Li et al. [19], and the proposed method. Following the allocation rules reported in the original studies, the methods of Fan et al. and Li et al. are adapted to the present case study. All methods are evaluated using the same total BESS power command, initial SOC and SOH values, unit parameters, and operating constraints. To provide a consistent basis for evaluating the effects of different power allocation strategies on the lifetime of individual energy storage units, the BLAST-Lite lifetime model for large-format lithium iron phosphate/graphite (LFP/Gr) batteries is used to calculate the SOH evolution and available-capacity fade of each unit during operation [25]. In the long-term simulation, the final SOC of each unit on one equivalent operating day is carried over as its initial SOC on the following day, while its SOH, available capacity, and retirement status are updated accordingly. An SOH threshold of 0.8 is used to define the end of life (EOL). The five units with the lowest initial SOH values are defined as the low-SOH group, and their annual SOH loss is calculated as the mean SOH decrease over 365 equivalent operating days. The cumulative total-command unmet rate is calculated as the cumulative energy deviation divided by the total command energy over 2500 equivalent operating days. The main results are presented in Table 5.

Table 5. Comparison of long-term operating performance under different power-allocation strategies.

Allocation Strategy	Time to First EOL (Equivalent Days)	Time to Second EOL (Equivalent Days)	Annual SOH Loss of Low-SOH Group (%)	Cumulative Total-Command Unmet Rate (%)	Average SOC Range
Proportional allocation	1271.7	2163.2	0.6075	5.0644	0.0195
SOC-margin-based allocation	1300.9	2205.1	0.6009	4.9173	0.0089
Health-aware rule-based power sharing [16]	1053.0	1785.4	0.6439	8.0554	0.4328
Dynamic-feedback SOC equalization [19]	1286.1	2179.3	0.6015	5.0027	0.0066
Proposed method	1439.6	2353.3	0.5761	4.4554	0.0159

As shown in Table 5, under the adopted degradation model and equivalent operating conditions, the first and second EOL events occur after approximately 1439 and 2353 equivalent operating days, respectively. Relative to proportional allocation, the corresponding times to EOL are extended by 13.20% and 8.79%. The time to the first EOL is extended by 36.71% and 11.93% relative to Fan et al.'s health-aware rule-based power-sharing method [16] and Li et al.'s dynamic-feedback SOC equalization method [19], respectively. The annual SOH loss of the low-SOH group is 0.57%, the lowest among the five methods. The cumulative total-command unmet rate is 4.45%, which is 12.02%, 44.69%, and 10.94% lower than those of proportional allocation, Fan et al.'s method, and Li et al.'s method, respectively. Li et al.'s method achieves the smallest average SOC range, indicating better SOC-balancing performance. Overall, under the same simulation conditions, the proposed method delays the onset of EOL among the low-SOH units and improves long-term command fulfillment while maintaining a relatively small SOC range among the units. The reported EOL times are comparative metrics obtained using the adopted battery

lifetime model and equivalent operating conditions and should not be interpreted as direct predictions of actual service life.

6.4.2. Power Redistribution Under Warning and Fault Conditions

To evaluate the response of the proposed strategy to abnormal operating states of individual energy storage units, Unit 1 is selected for warning- and fault-condition tests. The warning and fault events are separately triggered at 14.25 h during the strong-fluctuation period. Under the warning condition, the maximum power of Unit 1 is derated to 50% of its rated value; under the fault condition, the unit is isolated from operation. The same total power command, initial SOC values, and initial SOH values are used in all scenarios.

Figure 11 illustrates power redistribution before and after the warning and fault events. Following the warning event, the power of Unit 1 is limited to 0.53 MW. After the fault event is triggered, its executed power decreases to zero. Meanwhile, the remaining normal units adjust their outputs and undertake part of the displaced regulation task. These results demonstrate that the proposed method can achieve warning-state derating, fault isolation, and power redistribution according to unit-state information.

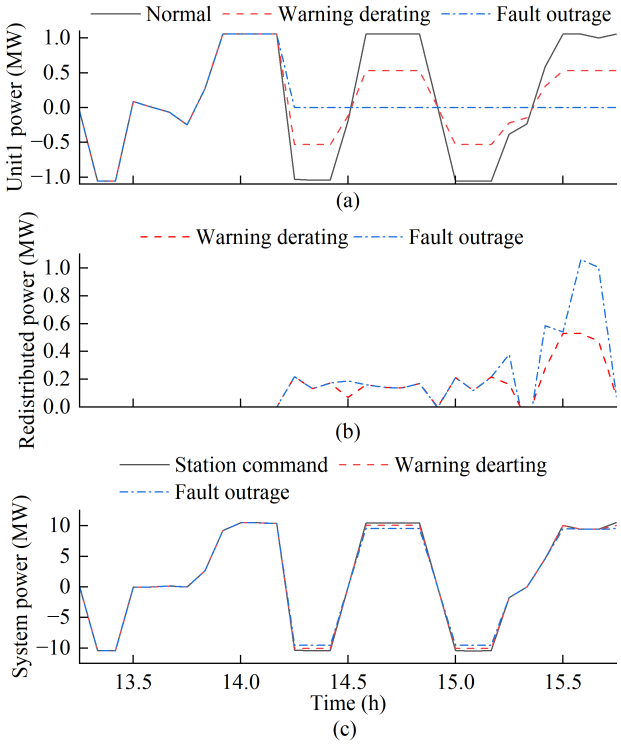


Figure 11. BESS power transfer under warning and fault conditions. (**a**) Unit 1 power; (**b**) Power redistributed to the remaining units; (**c**) Total BESS power.

The main performance metrics for the three operating scenarios are presented in Table 6. Under the warning condition, the regulation energy assigned to Unit 1 decreases by 1.317 MWh, of which approximately 55.3% is transferred to the remaining units. Under the fault condition, 46.2% of the regulation energy originally assigned to Unit 1 is reassigned to the remaining units. The warning and fault conditions reduce the upper system power limit to 10.07 MW and 9.54 MW, respectively. When the total power command exceeds the remaining available limit, the BESS cannot fully execute the command, resulting in power curtailment and corresponding tracking errors.

Table 6. Power-redistribution metrics under warning and fault conditions.

Operating Scenario	Maximum Power of Unit 1 (MW)	Post-Event Regulation Energy (MWh)	Energy Transferred to Remaining Units (MWh)	Unserved Energy (MWh)	Tracking RMSE (MW)
Normal operation	1.060	2.713	0	0	0
Warning-state derating	0.530	1.396	0.728	0.591	0.097
Fault isolation	0	0	1.254	1.460	0.233

Two operating modes are further considered: without dynamic feedback and with dynamic operating-limit feedback. In the mode without dynamic feedback, the BESS operating limits prior to the fault are retained. In the feedback mode, the updated available power and energy limits obtained at the lower level are fed back to the rolling optimization layer. The total control command is then recalculated according to the current available BESS capacity. The comparative results are presented in Table 7.

Table 7. Performance comparison of dynamic operating-limit feedback.

Feedback Mode	Command-Tracking RMSE (MW)	Tracking-Deviation Energy Ratio (%)	Unserved Command Energy (MWh)	Out-of-Band Deviation RMSE (MW)	SOC Range
Without dynamic feedback	0.233	2.651	1.460	2.453	0.409–0.877
Dynamic operating-limit feedback	0.042	0.143	0.076	2.559	0.420–0.879

With dynamic operating-limit feedback, the command-tracking RMSE decreases from 0.233 MW to 0.042 MW, representing a reduction of 81.9%; the tracking-deviation energy ratio decreases from 2.651% to 0.143%, representing a reduction of 94.6%; and the unserved command energy decreases from 1.460 MWh to 0.076 MWh, corresponding to a reduction of 94.8%. Meanwhile, the SOC values of all units remain within the safe operating range. The out-of-band deviation RMSE increases from 2.453 MW to 2.559 MW. This indicates that, as the available BESS capacity decreases, the rolling optimization model appropriately adjusts the requirement for tracking the grid power schedule to improve the executability of the total control command.

These results demonstrate that dynamic operating-limit feedback enables PV–BESS dispatch to respond promptly to changes in unit states and available regulation capability, thereby reducing control commands that exceed the actual operating limits. Consequently, a closed-loop coordinated dispatch process integrating state awareness, power redistribution, operating-limit updates, and rolling-horizon correction is established.

6.5. Computational Performance and Parameter Sensitivity Analysis

To evaluate the real-time computational capability of the proposed method, ten repeated timing tests were conducted for the complete control procedure in MATLAB R2024a. The average computation time for a single rolling-horizon optimization update was 4.12 ms, with a maximum of 9.14 ms. The average time required to decompose the complete command sequence was 26.46 ms, and the average computation time for a single state-aware power allocation step was 0.017 ms. The total computation time for one complete control cycle averaged 34.32 ms and reached a maximum of 47.46 ms. This maximum was

substantially shorter than the 300 s control interval adopted in this study, indicating that the proposed method can meet the computational-time requirement of the 5-min dispatch interval on the simulation platform and under the test conditions considered.

To evaluate the effects of parameter selection on the simulation results, sensitivity analyses were conducted for the objective-function weights λ_1–λ_4 of the rolling-horizon optimization model, the regularization weights μ_1–μ_4 and elastic-net mixing parameter α of the command decomposition model, and the SOH sensitivity coefficient β and warning-state derating factor γ_w used in BESS power allocation. Only one parameter was varied at a time, while the other parameters and constraints were kept unchanged. For the command decomposition tests, the same ten sets of random perturbation and noise scenarios were used for each parameter value.

Within the tested ranges of the objective-function weights, the PV utilization rate ranged from 99.47% to 99.86%, the grid power RMSE ranged from 6.80 to 7.05 MW, the BESS degradation cost ranged from 6353.76 to 6707.74 CNY, and the electricity sales revenue ranged from 130,674.66 to 130,960.45 CNY. All tested cases satisfied the operating constraints. When the command decomposition parameters were varied, the correlation coefficient of the high-frequency component ranged from 0.9787 to 0.9872. The RMSE values of the high- and low-frequency components ranged from 0.562 to 0.775 MW and from 0.599 to 0.811 MW, respectively. ADMM converged in all cases, and the BESS power commands remained within the rated power limits. As β increased from 1 to 3, the proportion of high-frequency energy assigned to units with higher SOH increased from 63.41% to 69.34%. When γ_w increased from 0.3 to 0.7, the energy redistributed to the other units decreased from 968.64 to 527.43 kWh, while the tracking RMSE decreased from 149.72 to 44.51 kW. These results indicate a trade-off between restricting the power of the warning-state unit and maintaining overall tracking performance. Based on these results, the parameter values listed in Table 2 were adopted. The complete results are provided in Tables 8–10, with the adopted values shown in bold.

Table 8. Sensitivity analysis of the objective-function weights in the rolling-horizon optimization model.

Parameter	Value	PV Utilization Rate (%)	Grid Power RMSE (MW)	BESS Degradation Cost (CNY)	Electricity Sales Revenue (CNY)
λ_1	100	99.467	6.799	6524.40	130,674.66
	200	99.741	6.942	6524.40	130,847.46
	300	99.856	7.021	6524.40	130,916.83
λ_2	100	99.856	7.047	6432.69	130,960.45
	150	99.741	6.942	6524.40	130,847.46
	200	99.641	6.871	6583.51	130,752.77
λ_3	10	99.741	6.898	6707.74	130,800.40
	50	99.741	6.942	6524.40	130,847.46
	100	99.741	6.993	6353.76	130,928.59
λ_4	0.2	99.741	6.940	6530.19	130,840.49
	1	99.741	6.942	6524.40	130,847.46
	5	99.742	6.951	6497.25	130,882.66

Note: Bold values indicate the parameter settings adopted in this study.

Table 9. Sensitivity analysis of the total BESS control command decomposition parameters.

Parameter	Value	High-Frequency Correlation Coefficient	High-Frequency RMSE (MW)	Low-Frequency RMSE (MW)
μ_1	0.20	0.9872 ± 0.0005	0.562 ± 0.012	0.599 ± 0.007
	0.25	0.9831 ± 0.0005	0.671 ± 0.012	0.712 ± 0.007
	0.30	0.9794 ± 0.0006	0.757 ± 0.013	0.800 ± 0.006
μ_2	0.045	0.9830 ± 0.0005	0.679 ± 0.012	0.719 ± 0.007
	0.055	0.9831 ± 0.0005	0.671 ± 0.012	0.712 ± 0.007
	0.065	0.9832 ± 0.0005	0.663 ± 0.012	0.705 ± 0.007
μ_3	0.012	0.9834 ± 0.0005	0.659 ± 0.012	0.712 ± 0.006
	0.015	0.9831 ± 0.0005	0.671 ± 0.012	0.712 ± 0.007
	0.018	0.9830 ± 0.0005	0.672 ± 0.012	0.712 ± 0.008
μ_4	0.007	0.9787 ± 0.0006	0.775 ± 0.013	0.811 ± 0.007
	0.008	0.9831 ± 0.0005	0.671 ± 0.012	0.712 ± 0.007
	0.009	0.9865 ± 0.0005	0.576 ± 0.012	0.628 ± 0.006
α	0.25	0.9840 ± 0.0005	0.655 ± 0.012	0.697 ± 0.008
	0.30	0.9831 ± 0.0005	0.671 ± 0.012	0.712 ± 0.007
	0.35	0.9822 ± 0.0005	0.688 ± 0.012	0.728 ± 0.007

Note: Bold values indicate the parameter settings adopted in this study.

Table 10. Sensitivity analysis of the state-aware power allocation parameters.

(a) SOH sensitivity coefficient β				
Value	**High-SOH energy share (%)**		**SOH–energy correlation**	
1	63.41		0.9811	
2	67.66		0.9978	
3	69.34		0.9865	
(b) Warning-state derating factor γ_w				
Value	**Warning-state unit power limit (kW)**	**Redistributed energy (kWh)**	**Tracking RMSE (kW)**	**Clipped energy (kWh)**
0.30	318	968.64	149.72	909.08
0.50	530	750.84	96.54	574.37
0.70	742	527.43	44.51	256.37

Note: Bold values indicate the parameter settings adopted in this study.

7. Conclusions

To address strong PV power fluctuations, large forecast errors, and state differences among individual energy storage units, this study develops an adaptive coordinated dispatch framework for a PV–BESS. Based on the total BESS control command generated through rolling-horizon optimization, the framework integrates robust command decomposition, state-aware power allocation, and dynamic operating-limit feedback. The main conclusions are as follows:

(1) A robust total-command decomposition method incorporating elastic-net regularization and abrupt-change protection is proposed. The method reduces the influence of occasional data anomalies on the decomposition results and prevents genuine strong fluctuations from being excessively smoothed. The correlation coefficient between the extracted high-frequency component and the reference dynamic component reaches 0.983, and the high-frequency fluctuation retention rate reaches 87.086%. The ablation study and comparative experiments confirm the effectiveness of the method in anomaly suppression and dynamic-feature preservation.

(2) A differentiated power allocation method considering the SOC, SOH, and fault status of individual energy storage units is developed. The method transfers high-frequency regulation tasks to healthier units, reducing the proportion of high-frequency regulation energy assigned to the low-SOH units from 50% to 34.2%. The long-term degradation comparison indicates that the proposed method can balance the protection of low-SOH units, long-term command fulfillment, and SOC balancing among the units.

(3) A closed-loop coordinated dispatch mechanism based on dynamic BESS operating-limit feedback is established. Under abnormal operating conditions, the proposed mechanism enables warning-state derating, fault isolation, and regulation-task transfer without violating the SOC limits. After dynamic operating-limit feedback is introduced, the command-tracking RMSE and unserved command energy are reduced by 81.9% and 94.8%, respectively. The upper-level dispatch model can therefore revise subsequent control commands according to the actual regulation capability of the BESS.

The proposed method was evaluated through MATLAB-based numerical simulations using actual PV operating data. Hardware-in-the-loop testing and experiments on an actual BESS have not yet been conducted. In addition, the long-term degradation results depend on the adopted battery aging model and equivalent operating conditions. Therefore, these results are intended mainly for comparing the relative lifetime-protection effects of different methods and evaluating the feasibility of the proposed strategy under the simulated conditions. They should not be interpreted as direct predictions of the actual service life or field operating performance of a BESS power plant. Future work will combine hardware-in-the-loop testing with long-term field operating data to further evaluate the effects of device dynamics, communication delays, temperature variations, and actual operating conditions on dispatch performance, lifetime protection, and the operating economics of the PV–BESS.

Author Contributions: Conceptualization, W.L.; methodology, B.Z., L.X. and J.J.; software, B.Z.; validation, J.H.; formal analysis, Y.B.; investigation, M.I.; resources, W.L.; data curation, J.J.; writing—original draft preparation, B.Z. and Y.B.; writing—review and editing, W.L. and L.X.; visualization, J.J.; supervision, J.H.; project administration, M.I.; funding acquisition, L.X. All authors have read and agreed to the published version of the manuscript.

Funding: This research was funded by the National Key R&D Program of China, grant number 2025YFE0103000.

Data Availability Statement: Restrictions apply to the availability of these data. The data were obtained from a third-party PV power plant and are available from the corresponding author with the permission of the data provider.

Conflicts of Interest: Author Wei Li was employed by Economic and Technological Research Institute, State Grid Xinjiang Electric Power Co., Ltd. The remaining authors declare that the research was conducted in the absence of any commercial or financial relationships that could be construed as a potential conflict of interest.

Abbreviations

The following abbreviations are used in this manuscript:

ADMM	Alternating direction method of multipliers
BESS	Battery energy storage system
BMS	Battery management system
EOL	End of life

LFP/Gr	Lithium iron phosphate/graphite
LMD	Local mean decomposition
PV	Photovoltaic
RMSE	Root mean square error
SOC	State of charge
SOH	State of health
VMD	Variational mode decomposition
WT	Wavelet transform

References

1. Barbieri, F.; Rajakaruna, S.; Ghosh, A. Very short-term photovoltaic power forecasting with cloud modeling: A review. *Renew. Sustain. Energy Rev.* **2017**, *75*, 242–263. [CrossRef]
2. Si, Z.; Yang, M.; Yu, Y.; Ding, T. Photovoltaic power forecast based on satellite images considering effects of solar position. *Appl. Energy* **2021**, *302*, 117514. [CrossRef]
3. Chung, H.C. The long-term usage of an off-grid photovoltaic system with a lithium-ion battery-based energy storage system on high mountains: A case study in Paiyun Lodge on Mt. Jade in Taiwan. *Batteries* **2024**, *10*, 202. [CrossRef]
4. Li, Q.; Wei, X.; Wang, J.; Chao, Y.; Li, Y.; Fan, H. Enhancing battery energy storage systems for photovoltaic applications in extremely cold regions: A brief review. *Energy Sustain. Dev.* **2024**, *81*, 101517. [CrossRef]
5. Belgibayeva, A.; Rakhmetova, A.; Rakhatkyzy, M.; Kairova, M.; Mukushev, I.; Issatayev, N.; Kalimuldina, G.; Nurpeissova, A.; Sun, Y.-K.; Bakenov, Z. Lithium-ion batteries for low-temperature applications: Limiting factors and solutions. *J. Power Sources* **2023**, *557*, 232550. [CrossRef]
6. Elkazaz, M.; Sumner, M.; Thomas, D. Energy management system for hybrid PV–wind–battery microgrid using convex programming, model predictive and rolling horizon predictive control with experimental validation. *Int. J. Electr. Power Energy Syst.* **2020**, *115*, 105483. [CrossRef]
7. Syed, M.A.; Khalid, M. Neural network predictive control for smoothing of solar power fluctuations with battery energy storage. *J. Energy Storage* **2021**, *42*, 103014. [CrossRef]
8. Yang, J.; Yang, T.; Luo, L.; Peng, L. Tracking-dispatch of a combined wind-storage system based on model predictive control and two-layer fuzzy control strategy. *Prot. Control Mod. Power Syst.* **2023**, *8*, 58. [CrossRef]
9. Lin, L.; Cao, Y.; Kong, X.; Lin, Y.; Jia, Y.; Zhang, Z. Hybrid energy storage system control and capacity allocation considering battery state of charge self-recovery and capacity attenuation in wind farm. *J. Energy Storage* **2024**, *75*, 109693. [CrossRef]
10. Bahloul, M.; Daoud, M.; Khadem, S.K. Optimal dispatch of battery energy storage for multi-service provision in a collocated PV power plant considering battery ageing. *Energy* **2024**, *293*, 130744. [CrossRef]
11. Huynh, A.N.-L.; Deo, R.C.; Ali, M.; Abdulla, S.; Raj, N. Novel short-term solar radiation hybrid model: Long short-term memory network integrated with robust local mean decomposition. *Appl. Energy* **2021**, *298*, 117193. [CrossRef]
12. Xiao, G.; Xu, F.; Tong, L.; Xu, H.; Zhu, P. A hybrid energy storage system based on self-adaptive variational mode decomposition to smooth photovoltaic power fluctuation. *J. Energy Storage* **2022**, *55*, 105509. [CrossRef]
13. Zhang, Y.; Wu, Y.; Li, L.; Liu, Z. A hybrid energy storage system strategy for smoothing photovoltaic power fluctuation based on improved HHO–VMD. *Int. J. Photoenergy* **2023**, *2023*, 9633843. [CrossRef]
14. Wu, X.; Wu, Y.; Tang, Z.; Kerekes, T. An adaptive power smoothing approach based on artificial potential field for PV plant with hybrid energy storage system. *Sol. Energy* **2024**, *270*, 112377. [CrossRef]
15. Zhang, J.; Hou, L.; Diao, X.; Yang, X.; Tang, P.; Cao, X. Power allocation method of battery energy storage system considering state balance in smoothing photovoltaic power fluctuations. *Front. Energy Res.* **2022**, *10*, 965812. [CrossRef]
16. Fan, F.; Xu, Y.; Feng, X. Rule-based health-aware power sharing for a multi-unit battery energy storage system. *Int. J. Electr. Power Energy Syst.* **2021**, *132*, 107208. [CrossRef]
17. Gao, X.; Wu, X.; Xia, Y.; Li, Y. Life extension of a multi-unit energy storage system by optimizing the power distribution based on the degradation ratio. *Energy* **2024**, *286*, 129598. [CrossRef]
18. Attia, E.M.; Abdelsalam, H.A.; Rashad, E.E.M. Energy management and SoC balancing of distributed batteries in AC microgrids using consensus tracking control. *Sustain. Energy Grids Netw.* **2024**, *38*, 101345. [CrossRef]
19. Li, S.; Xu, Q.; Fang, L.; Xia, Y.; Hua, K.; Meng, Y. Dynamic feedback-based active equalization control method for state of charge of battery energy storage in the power grid. *Electr. Power Syst. Res.* **2024**, *230*, 110201. [CrossRef]
20. Chen, G.; Xia, X.; Zhao, X.; Zeng, X.; Ouyang, T.; Feng, H. A balanced SOH–SOC control strategy for multiple battery energy storage units based on battery lifetime change laws. *Electr. Eng.* **2025**, *107*, 7725–7736. [CrossRef]
21. Cedeño, A.L.; López Ahuar, R.; Rojas, J.; Carvajal, G.; Silva, C.; Agüero, J.C. Model predictive control for photovoltaic plants with non-ideal energy storage using mixed integer linear programming. *Energies* **2022**, *15*, 6427. [CrossRef]

22. Cassano, S.; Sossan, F. Scheduling power-intensive operations of battery energy storage systems and application to hybrid hydropower plants. *Appl. Energy* **2025**, *386*, 125559. [CrossRef]
23. Zou, H.; Hastie, T. Regularization and variable selection via the elastic net. *J. R. Stat. Soc. Ser. B Stat. Methodol.* **2005**, *67*, 301–320. [CrossRef]
24. Boyd, S.; Parikh, N.; Chu, E.; Peleato, B.; Eckstein, J. Distributed optimization and statistical learning via the alternating direction method of multipliers. *Found. Trends Mach. Learn.* **2011**, *3*, 1–122. [CrossRef]
25. Gasper, P.; Saxon, A.; Shi, Y.; Endler, E.; Smith, K.; Thakkar, F.M. Degradation and modeling of large-format commercial lithium-ion cells as a function of chemistry, design, and aging conditions. *J. Energy Storage* **2023**, *73*, 109042. [CrossRef]

Disclaimer/Publisher's Note: The statements, opinions and data contained in all publications are solely those of the individual author(s) and contributor(s) and not of MDPI and/or the editor(s). MDPI and/or the editor(s) disclaim responsibility for any injury to people or property resulting from any ideas, methods, instructions or products referred to in the content.